JOURNAL OF MATERIALS SCIENCE 4 (1969) 179–188

Dislocation Reactions and Cavitation Studies in Melt-Grown Sapphire

C. A. MAY, J. S. SHAH
H. H. Wills Physics Laboratory, The University, Bristol, UK

Received 4 August 1968, and in revised form 2 September

The veiled region in Czochralski sapphire has been examined for defects by optical micrography, scanning electron microscopy, electron microprobe analysis and X-ray topography. High optical scattering in the veiled region is found to be due to a large number of cavities. Some dislocation reactions have been observed in the X-ray topographs. High strain fields associated with cavities are also revealed by the topographs indicating that they contain entrapped gas at high pressure. This pressure is three orders of magnitude greater than that predicted from surface tension considerations.

1. Introduction

It is widely known [1-3] that sapphire crystals grown by methods such as Czochralski pulling and electron beam zone refining often incorporate opaque or translucent regions, referred to as "veils". In these regions a large number of voids is present. However, little is known about the mechanism responsible for the formation of the veils. The work reported here concerns the examination of the defects in the veiled crystals by using newer techniques of scanning electron microscopy, X-ray topography and electron microprobe analysis. Optical microscopy is also used for the examination. An attempt is made to identify the origin of these defects.

Although the work reported is done on Czochralski crystals, the findings cited here should be relevant to crystals, grown from the melt by other methods.

2. Specimens

Two slices perpendicular to the growth axis from two crystals were examined. The slices were supplied by RRE Malvern (courtesy J. B. Mullin) and were from 14° crystals (i.e. crystals with the boule axis inclined at an angle of 14° from the c-axis) pulled from 99.999% Al_2O_3 melt contained in an iridium crucible in the presence of argon with 0.5 vol % oxygen ambient. The rate of pulling was 5 mm/h [2]. The general features of the veils observed in these slices were similar and all the observations cited here were common to both slices. Therefore, for the sake of clarity, coherence and brevity, a complete examination of only one of the slices is described here.

The general features of the specimen can best be understood by referring to a schematic sketch of the slice drawn in fig. 1a together with its stereogram in fig. 1b. The shaded portion in the sketch refers to the translucent region visible to the naked eye when holding the crystal to the light. This appears to reflect symmetry of the crystal possessing a more or less hexagonal form, with three clear arms corresponding to the $<1\bar{1}00>$ direction of the sapphire.

3. Optical Microscopy and Scanning Electron Microscopy

The crystal section was examined by both optical reflection and transmission microscopy after it had been polished and etched. As expected, both the examinations revealed that the scattering in the veiled region was most probably due to cavities present in that region. The size of the cavities varied from 15 to 60 μm diameter. Fig. 2 is a scanning electron micrograph of a single cavity. No faceting of the cavity walls was observed.

4. Electron Microprobe Analysis

Electron microprobe analysis was performed on the slice, essentially to look for inclusions of foreign phase and accumulation of impurities

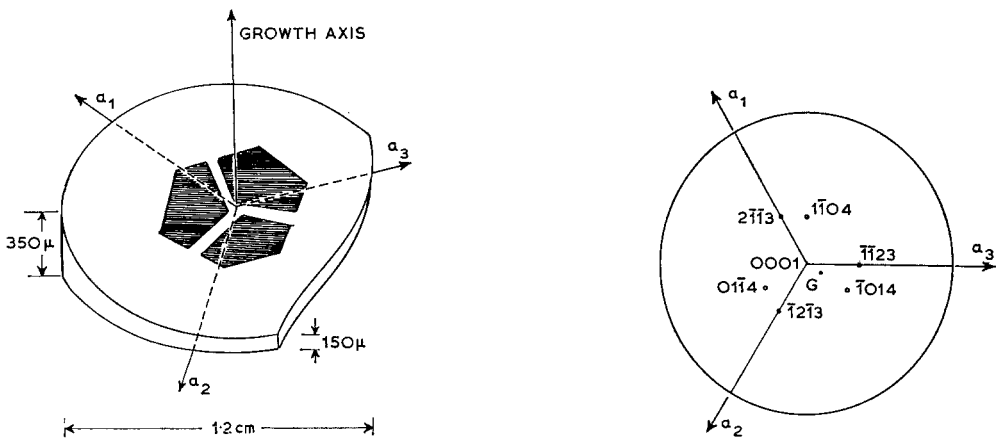

(a) (b)

Figure 1 (a) Schematic representation of the crystal slice showing configuration of the veil. (b) Corresponding stereographic projection.

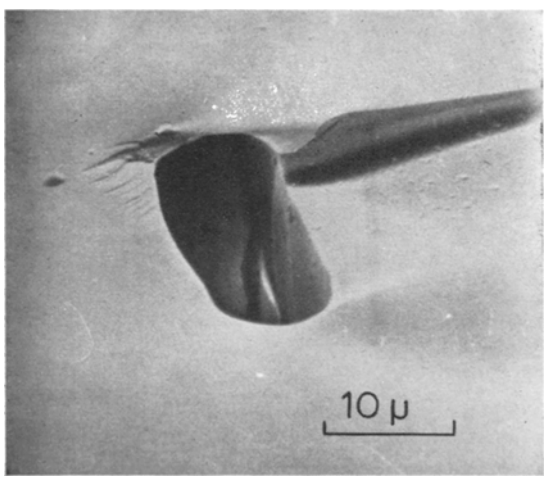

Figure 2 Scanning electron micrograph of a single cavity.

due to segregation. The analysis was performed on a JEOL (Japan Electron Optics Laboratories Co.) machine using LiF, quartz and kAP crystals. No impurity was detected in either the clear portion of the specimen nor in and around the cavities. Occasionally Si and C were found inside the cavities but these were thought to be small particles of SiC abrasive trapped in the cavities during polishing. Small particles were indeed seen in scanning electron micrographs and back scattered electron topographic pictures in the microprobe machine. Fortunately very few cavities contained foreign particles of SiC.

The conclusion from this analysis was that neither inclusions nor accumulation of impurities was present in the veiled region.

5. X-ray topography

A series of topographic experiments was embarked upon with the objective of determining the dislocation density and configuration around the cavities. Direct observation of dislocations in sapphire has been effected by the decoration technique [4]. X-ray topographical studies have been reported on Verneuil sapphire by Lommel and Kronberg [5] using the Berg-Barrett method, and on ruby using the Lang transmission method, by Belt [6]. We have chosen the Lang technique since dislocations in the bulk crystals may be studied, and the identification of Burger's vectors is easily carried out utilising different reflections.

5.1. Experimental Procedure

It was discovered that the best method of grinding and polishing the surface was to use only one grade of water lubricated emery paper (in this case 00 grade). The abrasive particles became progressively finer as grinding proceeded until a highly polished surface was obtained. Transferring to a finer paper invariably resulted in fresh pitting of the surface. Furthermore, diamond polishing was found unsuitable as it often produced scratches on the surface. The surface damage due to grinding was then removed with boiling phosphoric acid. The effective action with this etch is in the temperature range 210 to 270° C. Since the acid tends to decompose on heating

it was deemed expedient to use several fresh charges of it to ensure removal of damage or, as in later experiments, to achieve desired specimen thickness. In X-ray section topography, a technique described by Lang [7], images due to extraneous surface flaws can be readily distinguished. It was ensured by taking section topographs that complete removal of the surface damage was achieved.

Optimum thickness for a projection topograph depends upon the type of X-ray radiation and the maximum intensity criterion [8] namely

$$\mu t = 1 \qquad (1)$$

where μ is the linear absorption coefficient of the material for the radiation used and t is the specimen thickness.

In our case Mok_α radiation was used so that for sapphire $\mu = 13.4\ cm^{-1}$; therefore the optimum thickness is 0.75 mm. A preliminary exposure on a crystal of this thickness was carried out. Unfortunately the dislocation density was of such magnitude that considerable overlap of images prevented a meaningful interpretation. A significant feature of this topograph was a dark vertical band, in the middle, indicating an area of enhanced diffraction intensity. The observation implies that the crystal slice was warped, since the weakly diffracting extremities of the slice are not in the same favourable orientation. This was plainly unsatisfactory, therefore the crystal was resectioned carefully and etched to the considerably reduced thickness as shown in fig. 1a. The main body of the observations were taken from this thinned crystal.

The method of projection topograph permits resolution of fine detail from a single Laue reflected spot. Mok_α radiation was again used. $(\bar{1}\bar{1}23)$ and $(\bar{1}014)$ diffraction vectors were chosen as shown in fig. 1b. The above vectors represent the strongest reflection planes in sapphire and by systematic comparison of all six reflections an accurate appraisal of Burger's vectors may be performed.

5.2. Features of the X-ray Topographs

5.2.1. General Observations

The vertical magnification in all the topographs studied is very close to unity and the horizontal or lateral magnification is given by the expression [7].

$$M = \sec(\theta - \alpha)\sin\theta \qquad (2)$$

where θ is the Bragg angle and α is the angle between the Bragg plane and the specimen surface normal measured in the same sense as the deviation of the diffracted beam, The lateral dimension of the crystal is reduced by a factor $\cos(\alpha - \theta)$ in its topographic image.

Fig. 3 is a projection topograph of the crystal slice imaged from $(2\bar{1}\bar{1}3)$ planes. The dimensions of the crystal parallel to **g**, the diffraction vector, in the topograph are foreshortened by a factor of cos 26° (i.e. by 0.9) as discussed above. The region of high optical scattering is depicted here with remarkable clarity and incorporates high concentration of dark spots probably associated with the cavities in the region. The dark spots may of course be due to the inclusions but this is ruled out on the evidence of microprobe analysis.

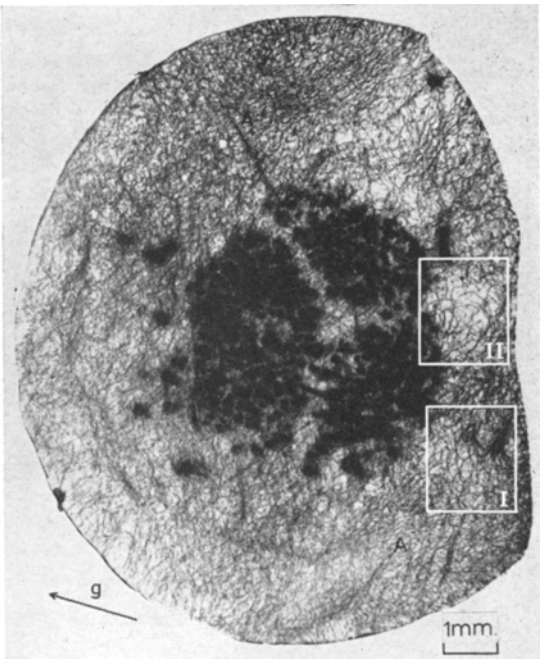

Figure 3 X-ray topograph of sapphire crystal Mok_α radiation $[2\bar{1}\bar{1}3]$ reflection.

The dislocation configurations outside the region of high optical scattering are well resolved particularly in the areas in the thinner part of the crystal designated by I and II. By counting the number of dislocations intersecting the thin edge of the crystal, the average density was estimated to be 7×10^3 lines/cm^2. This is comparable to other estimates in Czochralski sapphire [9]. It is

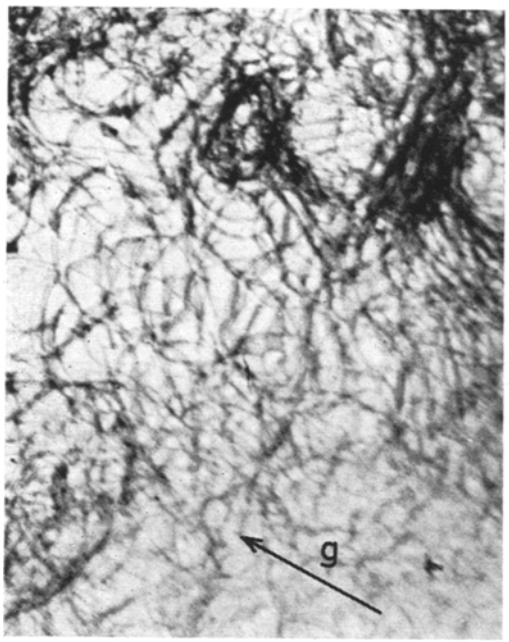

(a)

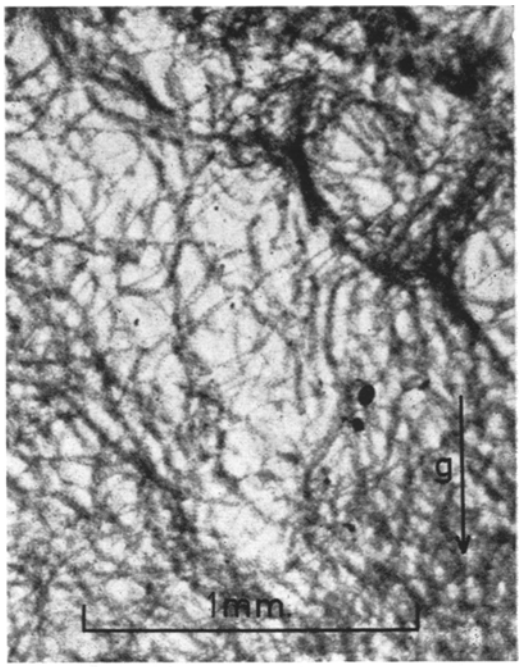

(b)

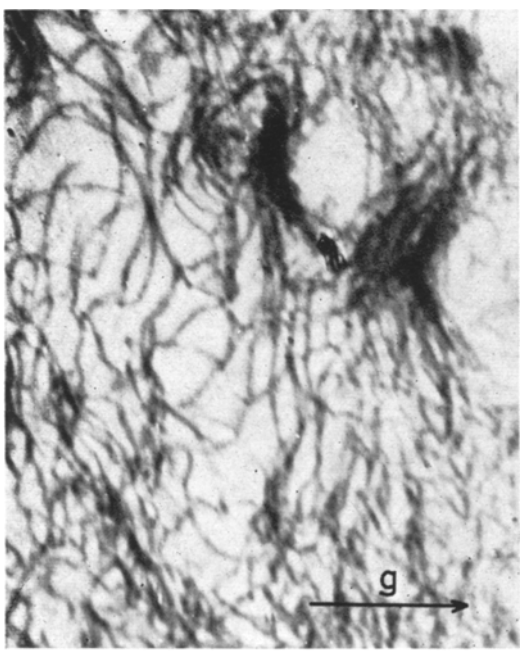

(c)

Figure 4 Segments of basal plane network. (a) $[2\bar{1}\bar{1}3]$ reflection. (b) $[\bar{1}2\bar{1}3]$ reflection. (c) $[\bar{1}014]$ reflection.

noted that the dislocation density varies by a factor of ten between the highest and lowest populated region. Allied with the inhomogeneity of the dislocation density there is an apparent lack of directionality, in contrast to the observation of Belt on ruby [6]. Only in the regions marked A is there a pronounced crystallographic alignment. The dislocations at the top of the fig. 3, for example, have an uninterrupted length of 4 mm along $[\bar{1}100]$. This suggests that they lie in the basal plane and possess a $[\bar{1}\bar{1}20]$ Burger's vector. This is substantiated by observing under the $[\bar{1}\bar{1}23]$ diffraction condition, when the image is wide and dense. These alignments may be interpreted as pure-edge dislocations constituting a low angle tilt boundary. However, crystallographic alignment is rare and a great majority of dislocations are curved, forming distorted networks and tangles.

5.2.2. Basal Networks

The existence of basal dislocations is well documented [4, 10-12]. The preponderance of these networks as observed in fig. 3 merely serves to confirm their stability in sapphire and to indicate their usefulness in lowering total dislocation strain energy of the crystal.

Fig. 4 shows an enlarged view of the area marked I in fig. 3 imaged under three reflecting

conditions. The contrast of a dislocation line is determined by the relative orientation of the diffraction vector **g**, Burger's vector **b** and a unit vector **n** parallel to the dislocation line. $\mathbf{g} \times \mathbf{b} = 0$ represents the zero contrast condition, but for pure edge dislocations to become invisible the condition $\mathbf{g} \times \mathbf{n} = 0$ must also be satisfied [13] since such dislocations create lattice distortion in two orthogonal directions. In the special case where the dislocation line is perpendicular to **g** and in edge orientation, a double image is often observed. Such double images are seen in fig. 4a indicating that they possess the $[\bar{1}\,\bar{1}\,20]$ Burger's vector. The alternate possibility that genuine dissociation has occurred must be discounted because a splitting of 15μm as observed here would certainly have been detected by electron microscopy [12].

Many triple nodes are also resolved in fig. 4. Close examination of fig. 3 and fig. 4 reveals large areas of planar dislocation network. The salient feature of fig. 4c is the large number of invisibilities that have occurred on imaging with $(\bar{1}014)$ planes. From this we conclude that the Burger's vector of these dislocations out of contrast is $[\bar{1}2\bar{1}0]$. This is indeed a structurally possible Burger's vector and is consistent with the generally accepted node forming reaction, namely

$$[\bar{1}2\bar{1}0] + [\bar{1}\,\bar{1}20] = [\bar{2}110]\,. \qquad (3)$$

Where these plane networks lie in screw orientation a twist boundary results [14]. The average mesh spacing here is estimated to be 50 μm corresponding to a lattice misorientation of 3 sec of arc.

Hexagonal networks observed here are typical of those in the crystalline materials possessing a threefold or sixfold symmetry axis. These are thought to form by intersection of basal slip dislocations [15]. Another suggestion is that they are grown in during solidification and form useful sinks for impurity segregation [14]. If the latter were so, an undisturbed network with uniform cell size would be expected. However, dense clusters and highly curved dislocations, observed in fig. 4, lead us to propose that the clusters arise from the interaction and entanglement of slip dislocations immediately following the solidification.

5.2.3. Dislocation Reactions

Fig. 5 shows an area of particular interest where the dislocation density is only 3×10^3 lines/cm^2 and average image overlap is minimal. The two figures 5a and 5b constitute a stereo pair taken from $[2\bar{1}\,\bar{1}3]$ and $[\bar{2}11\bar{3}]$ reflections respectively. Contrast conditions are identical since the same family of Bragg planes are diffracting, but the angle of projection differs by 2θ (i.e. 19° for $[2\bar{1}\,\bar{1}3]$). Hence by viewing these together, using a stereoscopic viewer (or alternatively by viewing fig. 5a with right eye and fig. 5b with left eye), a vivid impression of three dimensional dislocation configuration is obtained. Thus segments ab, bc are observed to lie on a plane deeply inclined to the surface of the crystal. Therefore bc could be interpreted as a forest dislocation hinged at nodes b and c, and extended rather like a catapult by the intersecting glide dislocation de. The situation is not quite so simple as this however. In figs. 5c and 5d the segment bc has been rendered invisible by both $[\bar{1}2\bar{1}3]$ and $[\bar{1}014]$ reflections. The segment ab is clearly contrasted for all three reflections. It follows that segment bc has a different Burger's vector from be and that this vector should be the common direction of the $[\bar{1}014]$ and $[\bar{1}2\bar{1}3]$ planes. Reference to the stereogram shows that the intersecting direction cannot be assigned rational indices. However, the $[0\bar{1}12]$ direction makes an angle of 9° to $[\bar{1}014]$ and 5° to $[\bar{1}2\bar{1}3]$. It is reasonable to assume that negligible contrast will result in both cases and that the Burger's vector of segment bc is thus $\frac{1}{3}[0\bar{1}12]$. Barber and Tighe [12] have proposed the existence of this Burger's vector from electron microscope observations. Also macroslip on the system $(01\bar{1}1)$, $[0\bar{1}12]$ has been observed in sapphire whiskers by Bayer and Cooper [16]. A puzzling feature of the node b is that the segment bd continues in contrast for a short distance beyond b both in fig. 5c and 5d although most of the segment be is out of contrast under these reflecting conditions. For this reason it is difficult to define unambiguously the nature of the interaction at b.

5.2.4. Cavity Contrast

Intense scattering from the defects in fig. 4 obscures any substructure that may be present around the dark spots. However, fig. 6a shows a part of the $[\bar{1}2\bar{1}3]$ topograph which is off peak, therefore not reflecting the full intensity. The immediate feature of interest is the clear band on each black spot perpendicular to **g**. This is reminiscent of strain contrast from precipitates in electron microscope pictures [17]. Assuming that the dark spots are due to cavities, the above feature may be explained as follows. The

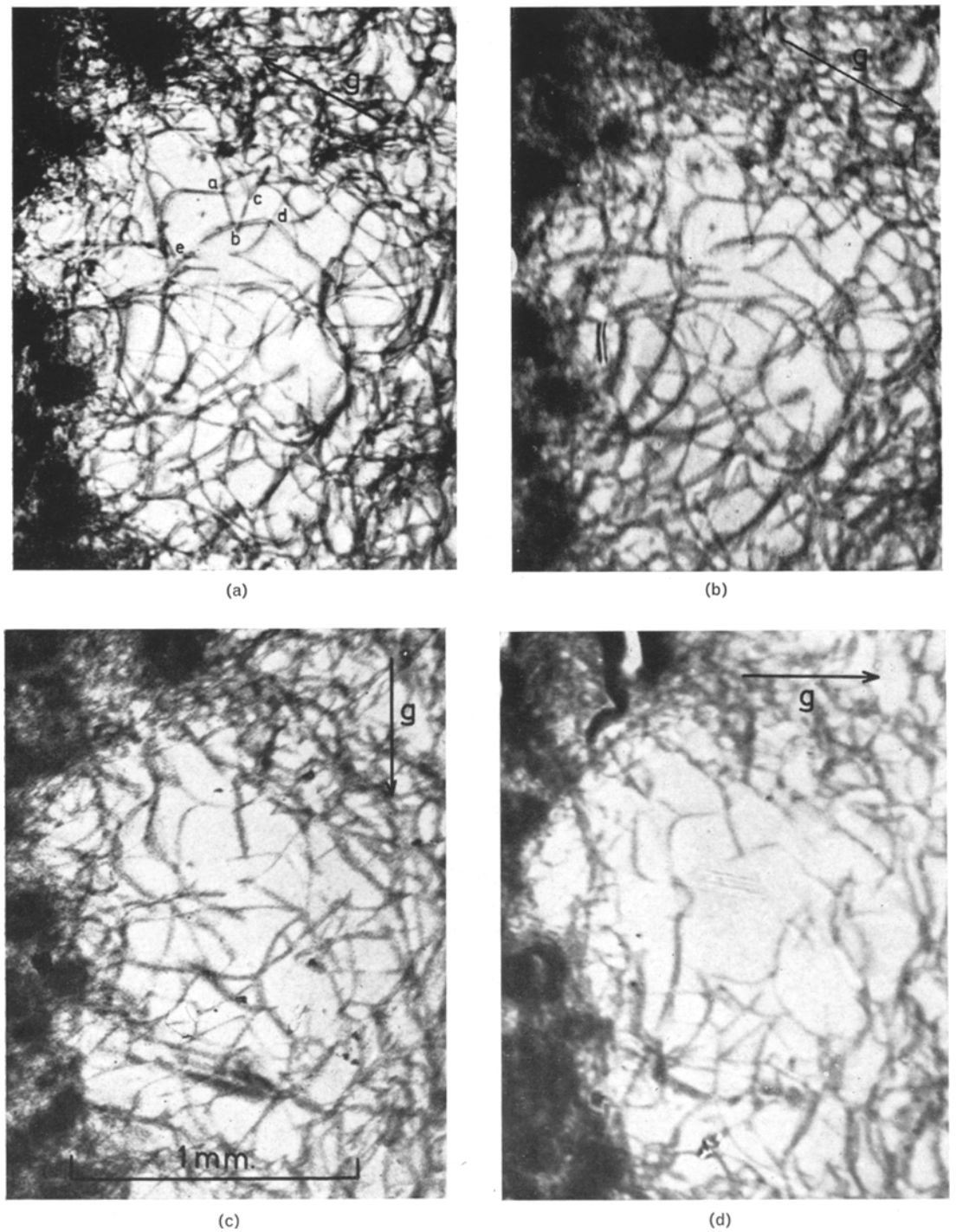

Figure 5 Three-dimensional dislocation reaction. (a) and (b) are stereo pair from $[2\bar{1}\bar{1}3]$ and $[\bar{2}113]$ diffracting planes. (c) $[\bar{1}2\bar{1}3]$ reflection. (d) $[\bar{1}014]$ reflection.

diffracting planes in the vicinity of each cavity are curved. This lattice strain varies from positive to negative on either side of the cavity. The low contrast band corresponds to the position where

the component of strain parallel to **g** is zero. The likely cause of this strain is hydrostatic pressure within the cavity. It is possible to estimate strain around a cavity from the contrast obtained in the X-ray topographs and hence estimate hydrostatic pressure within the cavity. One can assess the minimum Bragg plane bending which gives rise to detectable blackening on the photographic plate. This measure of strain at a known distance from the bubble permits one to use the expression for the radial strain around a cavity in terms of hydrostatic pressure. To estimate the limit of detectable strain from the topograph one makes direct comparison of the strain around a cavity with that around an edge dislocation. The bending of Bragg planes at a distance from the centre of stress may be assumed to be similar in both the case of an edge dislocation and a bubble under pressure. The strain field around an edge dislocation is given by the expression in cylindrical co-ordinates.

$$\epsilon = \frac{\mathbf{b}}{2(1-\nu)} \frac{\cos\theta}{r} \tag{4}$$

where ϵ is the strain at a distance r from the dislocation, **b** is the Burger's vector, ν is the Poisson's ratio (which is 0.32 for sapphire). Thus by substituting the value of r equal to half the image width of the dislocation, namely 5μm and $\cos\theta = 1$, a measure of the strain intensity is obtained. This value of ϵ may be substituted in the expression for strain round a spherical cavity (in an isotropic medium), namely

$$\epsilon = \frac{P}{2\mu}\left(\frac{r}{R}\right)^3 \tag{5}$$

where P is the pressure inside the cavity, μ is the elastic constant of the medium r, is the actual radius of the bubble (as obtained from the optical micrograph) and R is the radius of the topographic image of the bubble.

Fig. 6a is the topographic image of the same area

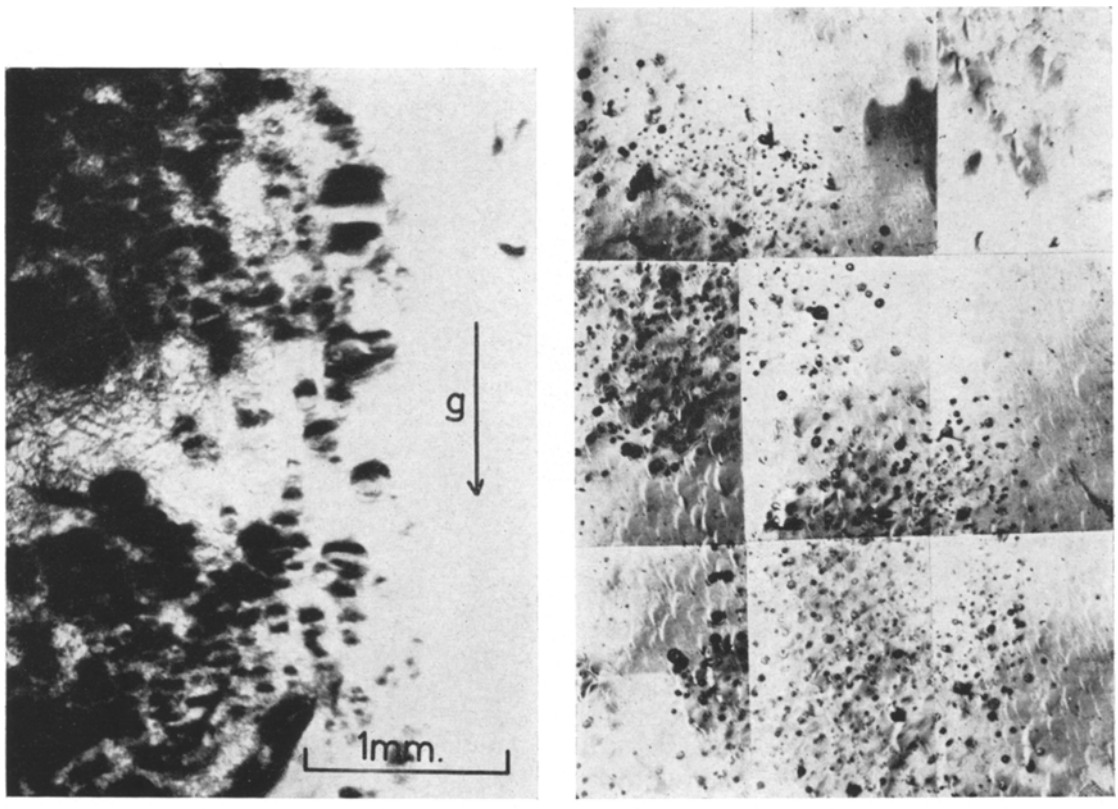

Figure 6 (a) X-ray topographs of spherical defects [$\bar{1}2\bar{1}3$] reflection. (b) Mosaic of the corresponding area—reflecting light micrograph.

as that shown in the optical micrograph of fig. 6b. Using half image width of 5μm for $[\bar{1}\bar{1}20]$ dislocation with $\mathbf{b} = 4.85$ Å, $\mu = 35 \times 10^5$ kg/cm^2 and a typical value of $r/R = \frac{1}{4}$, the pressure inside the bubble was found to be approximately 2000 atm.

Of course only an order of magnitude accuracy is claimed for the above calculation because (a) the equation 5 deals with a spherical bubble in an isotropic medium and (b) it is an oversimplification to say that the diffracting criteria around the radial and cylindrical centres of strain are the same.

6. Discussion

From the evidence presented here it is apparent that the high optical scattering associated with the veils is due to cavitation and not due to particle scattering. One must therefore, look for a mechanism responsible for the formation of voids in sapphire.

Cavitation can occur during crystal growth processes. It is reported that Czochralski sapphire formation of voids is associated with the speed of pulling and that voids are invariably formed if a crystal of dimater ~ 1 cm is pulled at a speed greater than 6 mm/h [2]. It seems likely therefore that the cavity formation is associated with the breakdown of the solid/liquid interface. One suggestion is that voids are formed by solidification of trapped, impure melt, due to constitutional supercooling and thereby incorporating solute trails ending in cavities as a result of contraction on solidification [2]. Elegant evidence for this cavity forming mechanism for mixed oxides such as ($CaO.WO_3$) [18] and ($3Y_2O_3 \cdot 5Al_2L_3$) [19] is available. No direct evidence associated with the above mechanism has been published for sapphire. Microprobe analysis on the specimen under consideration failed to detect any trace of solute segregation. Constitutional supercooling can of course be caused by dissolved gaseous impurities. The segregation coefficients of gaseous solutes are frequently small and as a result a large amount of segregation can occur at the interface. For a crystal growing in a near c-axis orientation, the deposition of basal layers will result in the development of a stepped interface defined by successive (0001) and $(01\bar{1}l)$ planes where $l = 0,1$ etc. The re-entrant corners between $(0\bar{1}1l)$ facets and the underlying basal plane would provide preferential entrapment centres for gaseous impurities, giving rise to interface instability. Adjacent $(0\bar{1}1l)$ and $(10\bar{1}l)$ facets intersect along a common $[1\bar{1}00]$ direction radiating from the centre of the growing interface. The corners so formed project into the melt and are less likely to act as favourable nucleation centres for dissolved gas. This could be the reason for cavity free $[1\bar{1}00]$ directions in the crystal as shown in fig. 1a, and for non-cellular distribution of the bubbles.

However, the large pressure of roughly 2000 atm inside the cavities as detected from the topographs cannot be explained if the gas bubble was nucleated in liquid as indicated in the above discussion. If a bubble is formed in a liquid, pressure inside is limited by surface tension and is $2\gamma/r$ where γ is the surface tension of liquid alumina (which is of the order of 700 dyn/cm) and r is the radius of the bubble. This is of the order of 1 atm. The enormous strain field associated with the cavities may be due to the growth of initially precipitated and stable bubble nuclei in the solid (crystal). Further work is in progress on the lines suggested by Speight [20].

Acknowledgement

The authors wish to thank J. R. Tesh for the electron microprobe work, H. E. Hinton and J. W. Heavens for the use of a scanning electron microscope, F. C. Frank, A. R. Lang and other colleagues for suggestions and help. Also financial support from SRC is acknowledged with thanks.

References

1. S. O'HARA, *J. Cryst. Growth* **2** (1968) 145.
2. B. COCKAYNE, M. CHESSWAS, and D. B. GASSON, *J. Materials Sci.* **2** (1967) 7.
3. W. CLASS, H. R. NESOR, and G. T. MURREY, Scientific Report No. 2. Contract A.F. 19(628)-4089 Materials Research Corporation Orangburg NY 1965.
4. D. L. STEPHEN and W. J. ALFORD, *J. Amer. Ceram. Soc.* **47** (1964) 81.
5. J. M. LOMELL and M. L. KRONBERG, Conf. Proc. "Direct Observations of Imperfections in Crystals" (St. Louis, 1960) p. 543.
6. R. F. BELT, *J. Amer. Ceram. Soc.* **50** (1967) 588.
7. A. R. LANG, *Acta Met.* **5** (1957) 358.
8. W. W. WEBB, Conf. Proc. "Direct observations of Imperfections in Crystals" (St. Louis, 1961) p. 588.
9. W. J. ALFORD, W. H. BAUER, and R. W. MATOLKA, Contract AF 19(604)8495 School of Ceramics, Rutgers, The State University, New Brunswick (1966).

10. R. SCHEUPLEIN and P. GIBBS, *J. Amer. Ceram. Soc.* **43** (1960) 458.
11. *Idem, ibid* **45** (1962) 439.
12. D. J. BARBER and H. J. TIGHE, *Phil. Mag.* **14** (1966) 531.
13. W. T. READ, "Dislocations in Crystals" (McGraw Hill, New York, 1953).
14. C. A. MAY and K. H. G. ASHBEE, *Phil. Mag.* **18** (1968) 61.
15. P. DELAVIGNETTE and S. AMELNIKS, *J. Nucl. Matls.* **5** (1962) 17.
16. P. D. BAYER and R. E. COOPER, *J. Materials Sci.* **2** (1967) 301.
17. M. F. ASHBY and L. F. BROWN, *Phil. Mag.* **8** (1963) 1083.
18. B. COCKAYNE, D. S. ROBERTSON, and W. BARDSLEY. *Brit. J. Appl. Phys.* **15** (1964) 1165.
19. W. BARDSLEY and B. COCKAYNE, Conf. Proc. ICCG (Boston, 1966). Supplement *J. Phys. and Chem. Solids* (1967) 109.
20. M. W. SPEIGHT, *Metal Sci. J.* **2** (1968) 73.

Book Reviews

Intermetallic Compounds

Edited by J. H. Westbrook

Pp. 663 (Wiley, New York, 1967) 285*s*

This is a most valuable book. The editor, an internationally recognised authority on the subject, has assembled twenty-nine chapters written by contributors from many parts of the world. (The book is *not* a conference proceedings.) These chapters are grouped under the headings: Introduction (one chapter); Bonding and Related Properties (six); Crystal Structure (six); Microstructure and Substructure (three); Formation, Stability and Constitution (three); Kinetics and Transformations (three); Properties and Applications (seven). The term *intermetallic compound* has been elastically interpreted to include phases with a substantial homogeneity range, and those subject to an order/disorder reaction.

The result is a remarkably complete, well-organised and readable survey of a very involved field, where much depends on systematic grouping of observations to prevent intellectual indigestion. The chapters on crystal structure, for instance, convey a very clear picture of current crystal-chemical ideas that govern the choice of crystal structure in terms of both geometrical and quantum-mechanical ideas. Again, the final group of papers ranges from mechanical behaviour to magnetic, electronic and superconductive properties.

While publication was in 1967, references only go up to 1964, which proves that the path of an editor is a stony one! The index, an important feature in a book of this type, is excellent: in addition to the usual name and subject indexes, there is also a separate index of compounds.

In all, this expensive book is worth its price and is one of those of which one can say without hyperbole that it should be in every metallurgical library.

R. W. CAHN

Damping of Materials and Members in Structural Mechanics

B. J. Lazan

Pp. 317 (Pergamon, London, 1968) 105*s*

In recent years increasing attention has been paid to the importance of damping as a material property and as an engineering property. Apart from Zener's classical text of 1948 there appears to be no book exclusively devoted to damping, and the author's coverage of his subject appears to be exhaustive. Although particular emphasis is placed upon engineering mechanics aspects, there is a comprehensive review of the atomistic or molecular mechanisms of damping. Significantly, one of the most valuable aspects of the book is a vast compilation of data and an extensive list of references, forming together one third of the book. The compilation includes data on metals,